Detection of Magnetic Field Polarity with NV^- Centers in Diamond Enabled by Magnetic Resonance Circular Dichroism

Fabrizio Moro

Department of Materials Science, University of Milano-Bicocca, Milano 20125, Italy.

ABSTRACT

Diamond with negatively charged nitrogen-vacancy (NV^-) colour centers is a promising material system for quantum sensing applications and in particular for magnetometry. The sensing protocol leverages on optically detected magnetic resonance (ODMR) technique which provides high sensitivity to magnetic field magnitude and orientation from post-processing analysis of the resonance frequencies. A direct access to the magnetic stray field polarity would be appealing for the study of physical phenomena and applications where real-time detection of static and dynamic magnetization is required. Here, a new phenomenon named ODMR circular dichroism (ODMR-CD) is observed and shown to directly correlate the sign of the magnetic resonance spectral lines to the magnetic field polarity as result of circular dichroism of the exciting microwave radiation. A model is introduced to explain the mechanism underlying for ODMR-CD along with a *proof-of-concept* for real-time detection of magnetization switching.

INTRODUCTION

Quantum sensors are devices that leverage the principles of quantum mechanics to measure physical quantities with unprecedented precision and sensitivity with respect to the classical counterparts. There is a variety of quantum sensors based on superconductors, cold atoms, topological insulators to name a few, each with its own pro and cons in terms of sensitivity and spatial resolution. Negatively charged nitrogen-vacancy (NV^-) color centers in diamond crystals[1]

stand out because of their unique properties such as chemical, electrical and optical stability[2] as well as long spin coherence times at room temperature.[3] These exceptional properties make NV^- centers suitable for precise measurements of magnetic fields,[4] electric fields, [5] temperature,[6] and pressure.[7] Thus, NV^- centers in diamond represent a platform for applications across various fields such as quantum information,[3, 8] biological imaging,[9] nano MRI,[10] navigation[11], materials science[12] as well as for the exploration of novel phenomena in physics such as topological currents[13] and magnetic skyrmions.[14]

Particularly promising is their use in quantum magnetometry[15, 16] with magnetic field sensitivity down to pico-tesla,[1] as well as quantum imaging[15] with spatial resolution scalable down to nanometers. Magnetic field measurements are possible because the separation between the magnetic resonance frequencies of the NV^- spin ground state (S=1) increases linearly with the intensity of the magnetic field. Furthermore, the four inequivalent quantization axes of the NV^- centers due to the diamond tetrahedral symmetry enables the reconstruction of the magnetic field directions.[17] The technique employed is called optically detected magnetic resonance (ODMR) and relies on the detection of changes in the fluorescence upon magnetic resonance condition.[18-20] From the fitting of resonance peaks, the magnetic field vector magnitude and directions can be reconstructed.[17]

Unfortunately, the sign of the ODMR spectral lines is inherently independent on the magnetic field directions. Furthermore, the indirect and complex spectral analysis of the ODMR spectra hinders direct access to the magnetic field polarity as well as its real-time detection.

Here, a method is implemented which relies on a new effect dubbed for the first time ODMR circular dichroism[21] (ODMR-CD) where the spectra are recorded by demodulating an oscillating magnetic field in combination with linearly polarized microwaves. The locking of the modulation phase to the spin transitions enables to discern between different spin transitions, and to detect directly magnetic field polarities simply by reading-off the sign of the ODMR-CD spectral lines.

In the following, the ODMR-CD mechanism in a microdiamond with NV^- centers is investigated, and a model is introduced to explain the phenomenology. Finally a proof-of-concept for real time detection of slowly switching magnetic field directions is provided.

RESULTS AND DISCUSSION

Figure 1a shows the molecular structure of a NV^- center with respect to the crystal frame x_C, y_C, z_C and the lab frame x_L, y_L, z_L. The nitrogen atom can replace any of the 4 carbon sites in the tetrahedron, thus providing four inequivalent NV^- centers each with its own spin quantization axis. In **Figure 1b** is reported the Jablonski diagram with the S = 1 ground and excited states which are both zero-field split by both by axial (D) and rhombic (E) distortions. In zero magnetic field the 4 NV^- site are magnetically equivalent, however when an external magnetic field is applied the energy levels are split by Zeeman interaction and each NV^- site experiences a different magnetic field projection thus resulting in 4 doublets. The nuclear spin of ^{14}N contributes to a further splitting of the levels for each doublet.

Optical pumping with green light (532 nm) of the ground state $^3A_2$ to vibronic levels of ^3E leads to spin conversing radiative decay back to the ground state emitting photons in the red region of the electromagnetic spectrum. The $^3E(m_s = \pm 1)$ states mostly decay to the $^3A_2(m_s = \pm 1)$ ground state but a significant portion decays non radiatively to the singlet ^1A. These nonradiative transitions occur more rapidly from the $^3E(m_s = \pm 1)$ states than from $^3E(m_s = \pm 0)$. Singlet-singlet transition $^1A_1 \rightarrow {}^1E$ takes place with almost all the energy being transferred non-radiatively, a small portion of the transitions occur via emission of infrared radiation. Finally, nonradiative transitions from the ^1E singlet level to the triplet ground state $^3A_2$ occur with roughly equal transition probabilities. As result of the differences between the radiative and nonradiative transition rates of the $^3E(m_s = 0)$ and $^3E(m_s = \pm 1)$ states, after several excitation-relaxation cycles the population of the NV^- centers in the triplet ground state results strongly polarized in the $^3A_2(m_s = 0)$ sublevel. Under this condition,

the resonant excitation of the m_s states with powerful microwaves radiation saturates the $m_s = \pm 1$ states leading to a depolarization of the $^3A_2$ ($m_s = 0$) level, with a consequent quenching of the photoluminescence. Thereby, magnetic resonance transitions can be detected by monitoring the photoluminescence signal as function of a microwave frequency, thus providing the ODMR spectrum.

The scheme of ODMR technique is shown in **Figure 1c**, and further details of the set-up are given in the section METHODS. In a nutshell, a green laser beam is reflected by a dichroic mirror and focused on a diamond microcrystal mounted on a microstripline. Photoluminescence is detected through the objective, the dichroic mirror and it is focused on a photodiode. The current signal is low-noise amplified and fed into a lock-in amplifier and/or oscilloscope interfaced with a PC for data acquisition.

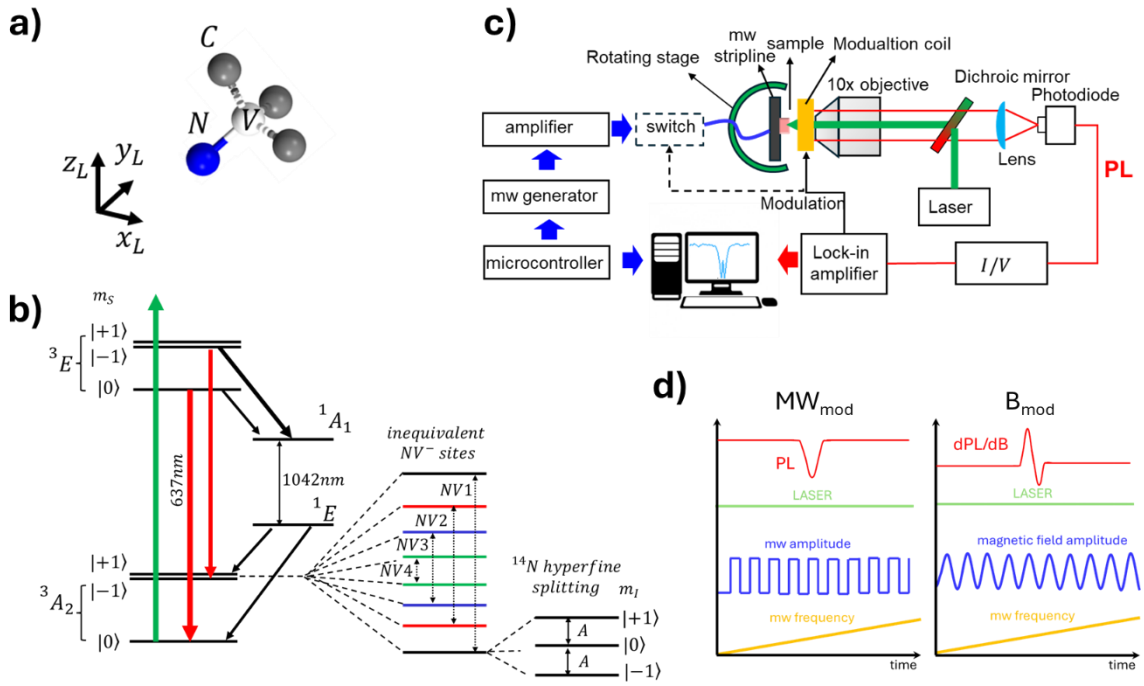

Figure 1 a) Structure of a NV^- center in the diamond crystal and laboratory frames. **b)** Energy level diagram of a NV^- center (S = 1) with axial and rhombic zero field splitting D = 2870 MHz and E = 7 MHz respectively and ^{14}N hyperfine interaction A. Arrows thickness stands for different transitions probabilities. Splitting of the $m_s = \pm 1$ sublevels due to inequivalent NV$^-$ sites is also

shown. **c)** Scheme of the ODMR set-up spectra with magnetic field modulation (B_{mod}) and microwave modulation amplitude (MW_{mod}, see components with dashed lines.) **d)** Detection scheme for ODMR with MW_{mod} and B_{mod} (see METHODS).

Figure 2a reports the high resolution experimental spectrum recorded with magnetic field modulation (B_{mod}) for an arbitrary angle. Four pair of peaks corresponding to the four inequivalent NV^- centers (NV1, NV2, NV3, NV4) are clearly distinguished symmetrically distributed around the frequency D = 2870 MHz. These peaks are also observed in the ODMR spectrum recorded directly with an oscilloscope hence without modulation field (bottom spectrum). The resonant lines are in-homogeneously broadened as well as broadened by N hyperfine interaction. The latter can be clearly seen for the inner pairs of peaks with three resolved evenly spaced resonances corresponding to electron-nuclear spin transitions shown in **Figure 1b**. The sign of the first derivative signals of the four doublets is found to be opposite for the resonance lines on the left and right with respect to the center of gravity of the spectrum with the pattern $+, +, +, +, -, -, -, -$.

The spectrum has been simulated by first calculating the frequency resonances for left (σ^-) and right (σ^+) microwave circular polarization for the transition $m_s = 0 \rightarrow +1$ and $m_s = 0 \rightarrow -1$ respectively and then calculating the dichroic spectrum $\sigma^+ - \sigma^-$ (see METHODS). The simulation is in satisfactory agreement with the experimental spectrum, and in particular it fully reproduces the sign pattern of the first derivative signals.

The ODMR spectrum in **Figure 2a** (grey line) recorded directly with an oscilloscope shows eight dips at the same resonant frequencies as for the spectrum recorded with the lock-in detection. The quenching in photoluminescence for all the four pair of peaks is a fingerprint for microwave absorption resulting in depopulation of the $m_s = 0$ state in favor of the -1 and +1 states. Conversely, an increase of photoluminescence would have corresponded to photon emission, hence

to transitions between energy levels with out-equilibrium population. Based on these observations the pattern $+,+,+,+,-,-,-,-$ in the ODMR spectrum in **Figure 1a** cannot be explained with transition from out-of-equilibrium population, instead it can only be explained with ODMR – CD.

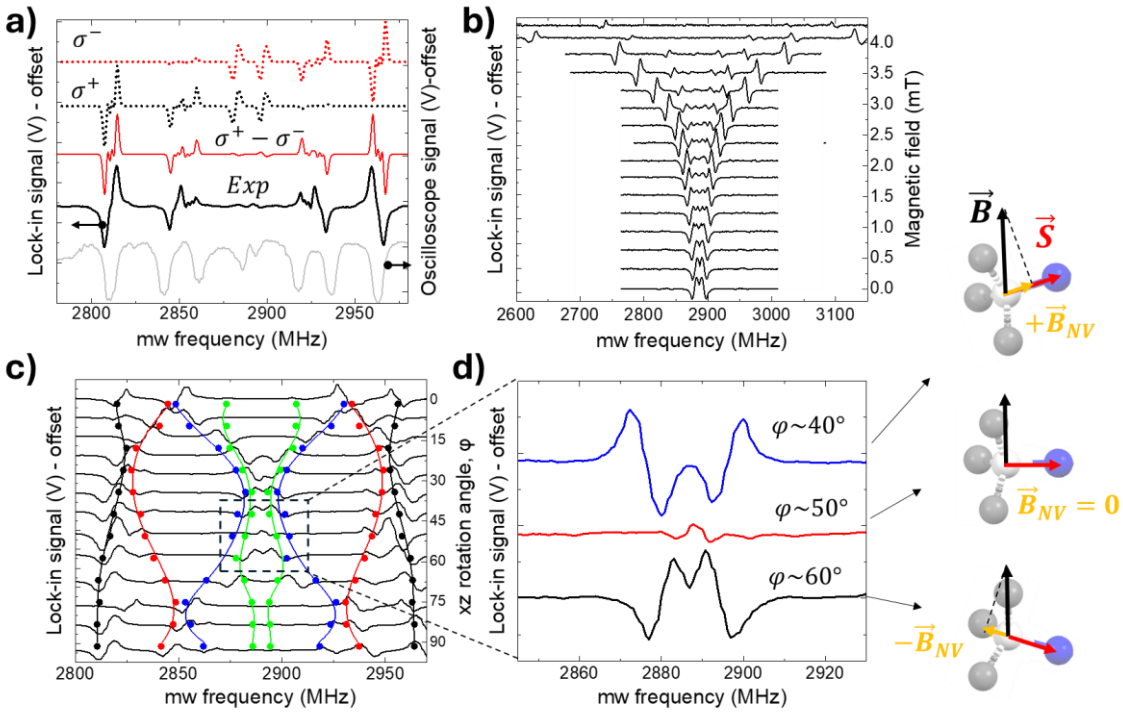

Figure 2 a) Experimental spectrum recorded for an arbitrary angle, $\varphi = 80°$ in the xz plane of the laboratory frame with external magnetic field $B \sim 3.2\ mT$ (step = 0.5MHz) along with the simulations of the spectra with right and left circularly polarized microwave radiation and their difference, i.e. dichroic spectrum. For comparison, the ODMR spectrum recorded directly with an oscilloscope is reported (grey line). **b)** Magnetic field dependent spectra for B varying from 0 mT (bottom spectrum) to 4 mT (top spectrum). **c)** ODMR - CD by rotating a permanent magnet (B ~ 3mT) in the xz laboratory plane. The dots are the extracted microwave resonance frequencies from the simulations of the ODMR spectra in **Figure S1** and the continuous lines are the interpolations. Color code: NV1 = black dots, NV2 = red dots, NV3 = blue dots, NV4 = green dots. **d)** Zoom of ODMR-CD peaks around the frequency range ~ D and for $40° < \varphi < 60°$. Inset: visualization of the applied field B and its projection B_{NV} on an NV^- spin quantization axis S for the angles $\varphi = 40°, 50°$ and $60°$. The switching of the magnetic field projections B_{NV} on a NV^- center from parallel to antiparallel to S is observed.

In order to achieve a deeper understanding of the ODMR-CD effect, the lock-in detection was performed with both modulation of the microwave signal amplitude (MW_{mod}) and of the magnetic field amplitude (B_{mod}) under different conditions. First of all, the spectra were recorded as function of the applied magnetic field (**Figure 2b**). At zero field the B_{mod} spectrum, reveals two first derivative signals with opposite sign as result of the fine rhombic splitting (E ~ 7 MHz) of the ±1 states. It is worth noting that at zero field the lock in signal results from the modulation of background magnetic field (i.e. earth magnetic field). By increasing the magnetic field the two peaks depart linearly in opposite frequency directions all the way up to 4 mT, and split in 4 doublets due to the different projections of the magnetic field on the 4 possible coordination of the NV^- centers in diamond. The sign of each resonance peak is consistently linked to the spin resonance transition, either 0 → +1 or 0 → -1, across the whole spanned microwave frequency and magnetic field ranges. It is worth noting that no level crossings occurs in the magnetic field range investigated which could have switched the transition from absorptive to emissive.[22] Indeed the level crossing between $m_s = 0$ and -1 is expected for magnetic field larger than 50 mT depending on the crystal orientation.[23]

Angular dependent studies were performed both in B_{mod} (**Figure 2c**) and MW_{mod} (see **Figure S1**) and by rotating a permanent magnet in the $x_L z_L$ laboratory plane (that is around the y_L axis) and recording ODMR spectra for different angles φ at fixed magnetic field B ≈ 3 mT. With this experiment, it is investigated the correlation between the first derivative sign and the 0 → +1 or 0 → -1 spin transitions in the magnetic switching regime, that is the regime where the magnetic field components ($\vec{B}_{NV}$) along the quantization axis of each of the four inequivalent NV^- centers turns from parallel to $\vec{S}$, to perpendicular and finally it switches to antiparallel direction with respect to $\vec{S}$.

The results reported in **Figure 2c** show that the resonance frequencies of the four doublets moves smoothly with the angle φ in a not trivial manner. The orientation of the microcrystal is random thus hindering a simple understanding of the particular pattern followed by the 4 doublets especially

for the B_{mod} spectra where the intensities of some peaks appear to decrease within a certain angle range (i.e turning points). Therefore, the ODMR spectra in MW_{mod} were simulated to extract the resonance frequencies for each spectrum and then overlayed to the ODMR spectra in B_{mod} for comparison (**Figure 2c**). The only fit-parameters were the Euler angles (α, β, γ) of the crystal frame relative to the laboratory frame by keeping the molecular frame fixed to (45° 54° 0) with respect to the crystal frame (**Table S1** and METHODS). The road map in **Figure 2c** shows that the outer resonance frequencies correspond to inequivalent NV^- center NV1 and NV2 which experience the largest magnetic field projection $\vec{B}_{NV}$. The weak angular dependence suggests that the magnetic field is mostly spinning around NV1 spin axis thus maintaining the magnetic field projection mostly constant. The remaining three pairs have smaller magnetic field projections, and experience a much larger resonance frequency shifts. For $\varphi \sim 30°$ the NV1 / NV2 and NV3 / NV4 resonances overlap and only four peaks can be distinguished. For $\varphi \sim 50°$ the inner resonances (NV3 and NV4) shift towards the center of gravity of the spectrum and after a critical angle the resonance lines re-emerge with an apparent inverted signs, that is (+,-) to (-,+) from 40° to 60°. A close look of the spectra in the range $\varphi \sim 40° - 60°$ (**Figure 2d**) reveal that the signal intensities for NV3 and NV4 decreases to the floor noise level. This effect is due to the fact that near the energy range of D, hence $B_{NV} \sim 0$ mT, the 0 → +1 and 0 → -1 transitions occur regardless of the microwave left of right polarization. Thus the calculated $\sigma^+ - \sigma^-$ spectrum results into a vanishing ODMR-CD signal. This phenomenon can be explained by the fact that the energy levels m_s = +1 and -1 are mixed in the frequency region near D and therefore they are no longer *good* quantum numbers.[24] Under this condition, the selection rules for spin transition are relaxed, and both transitions 0 → -1 and 0→ +1 occur independently of the microwave polarization (**Figure 3a**).

From a geometrical/structural viewpoint the quenching of the dichroic signal at the turning point for NV3 and NV4 can be explained by considering the magnetic field projection $\vec{B}_{NV}$ on the NV^- quantization axis, $\vec{S}$ (see inset **Figure 2d**). The Euler angles obtained from the simulations provide a

complete picture of the projections $\vec{B}_{NV}$ of the magnetic field along each NV$^-$ axis, thus enabling the visualization of $\vec{B}_{NV}$ with respect to the quantization axis, and to find its correlation with the ODMR-CD spectra. The magnetic field B, was rotated starting from $+\vec{B}_{NV}$ parallel to $\vec{S}$. When B is exactly perpendicular to one of the spin axis its projection $\vec{B}_{NV}$ is zero. For larger angles the projection reverses sign and the effective magnetic field is $-\vec{B}_{NV}$ and thus anti-parallel to $\vec{S}$. The selection rules for spin transitions are reversed by inversion of the magnetic field, and the spin transition induced by (σ^-) and (σ^+) are swapped as shown in **Figure 3b**. It turns out that the sign of the ODMR-CD lines depends on the relative orientation of B_{NV} and on the circular polarization according to the rules summarized in **Figure 3b**. At this point the mechanism for ODMR-CD manifests itself as emerging from the locking of the magnetic field modulation phase, and hence of the sign of the first derivative signal, to the electron spin transition.

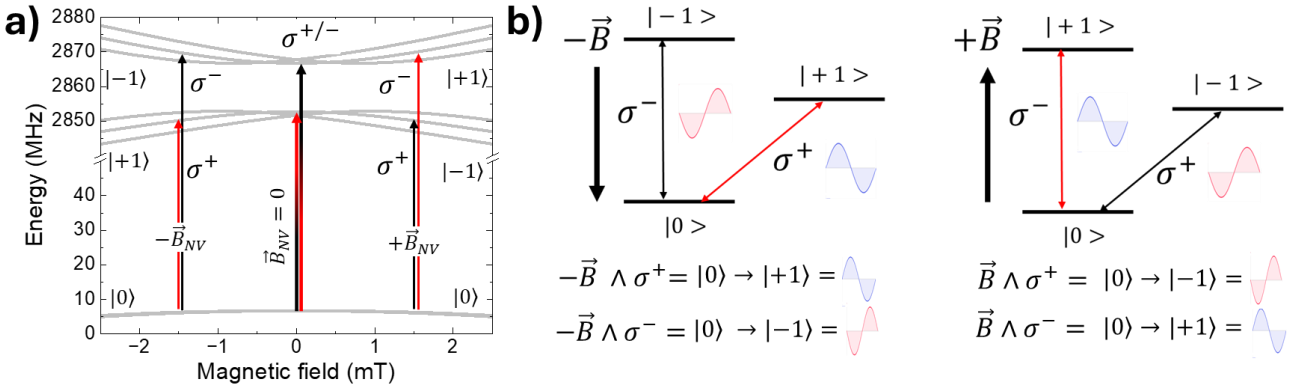

Figure 3 a) Effect of circularly polarized spin transitions going from positive to negative magnetic fields passing through the regime near B = 0 mT where the m_s states ±1 are not *good* quantum numbers and spin transitions occurs regardless of the microwave polarization $\sigma^{+/-}$. **b)** Relation between the magnetic field directions, spin transitions, circular polarizations and the sign of the first derivative ODMR-CD peaks.

THEORY OF ODMR – CIRCULAR DICHROISM

When a microwave $B_1 \sin(\omega_0 t + \phi_0)$ with magnetic field B_1, frequency ω and phase ϕ_0 is scanned trough the region of resonances of a spin system, an absorption or emission of microwaves occurs generating a change in the amount of microwave power in the transmission line as well as a change in the photoluminescence (PL). The latter is used for detection of spin transitions in ODMR. When the spin system is placed in an external magnetic field (B_0) and a small oscillating magnetic field $B_m \sin(\omega_m t + \phi_m)$ is applied, the energy levels of the spin system are modulated and the photoluminescence signal oscillates at the same frequency. Lock-in phase sensitive detection is based on a mixer which multiplies the reference oscillating field and the PL signal, and after appropriate low pass filtering enables to extract a first derivative like signal with large suppression of background noise.

The effect of modulation field on the carrier microwave is shown in **Figure 4a** where ΔE indicates the difference between the microwave amplitude off and on resonance condition. For comparison, the effect of modulation microwave amplitude is also shown (**Figure 4b**). The magnetic field modulation is transformed to PL modulation by conversion of the field $B_m \sin(\omega_m t + \phi_m)$ to a complex signal $F(\omega)$ which is a superposition of the fundamental modulation frequency ω_m and n harmonics[25]:

$$F(\omega) = \sum_{n=0}^{\infty} [a_n(\omega) \cos n\omega_m t + b_n(\omega) \sin n\omega_m t] \quad (1)$$

Each point of the PL signal can be describe by these terms where at the inflection point is composed mainly by the fundamental term $b_n(\omega) \sin n\omega_m t$, at the maximum peak by the second harmonic $a_2(\omega) \cos 2\omega_m t$ and for any other point by their combinations.

The only term responsible for the sign of the first derivative signal is the fundamental term $b_n(\omega) \sin n\omega_m t$ which is opposite for opposite sides of the absorption lineshape, whereas all the other terms and constants are always positive.

Thus, the first derivative signal is:

$$S(\omega < \omega_r) \propto +sin\,(\omega_m t + \phi_m); \quad (2a)$$

$$S(\omega > \omega_r) \propto -sin\,(\omega_m t + \phi_m); \quad (2b)$$

where S indicates the PL signal, ω_r is the resonance frequency and ϕ_m the modulation phase. Depending on ϕ_m the sign of the first derivative of the lock in signal can be shifted from positive to negative and viceversa. For $\phi_m = \frac{\pi}{2}$ and $\phi_m = \frac{3}{2}\pi$, $S \equiv S_+$ and $S \equiv S_-$ respectively.

The modulation of the microwave field B_o with the oscillating field $B_m \sin\,(\omega_m t + \phi_m)$ under resonance condition (**Figure 4a**) can be described by their convolution:

$$\Gamma \propto S(\omega_m) \otimes B_o(\omega); \qquad (3)$$

The linearly polarized electromagnetic wave can be expressed as superposition of left and right circularly polarized on the basis states:

$$\sigma^- \equiv \{\vec{B}_x; \vec{B}_y\} = \left\{\frac{B_0}{\sqrt{2}}\cos\,(kz - \omega t + \phi_0); -\frac{B_0}{\sqrt{2}}\sin(kz - \omega t + \phi_0);\right\} \text{(4a)}$$

$$\sigma^+ \equiv \{\vec{B}_x; \vec{B}_y\} = \left\{\frac{B_0}{\sqrt{2}}\cos\,(kz - \omega t + \phi_0); +\frac{B_0}{\sqrt{2}}\sin(kz - \omega t + \phi_0);\right\} \text{(4b)}$$

The sign of the B_y component depends on polarization direction and when convoluted with $S_{+,-}(\omega_m)$ provides a 0° or π phase shift for σ^- and σ^+respectively, and hence a reversal of the PL signal.

$$\Gamma_+ \propto S_+(\omega_m) \otimes \sigma^-(B_y) \quad (5a)$$

$$\Gamma_- \propto S_-(\omega_m) \otimes \sigma^+(B_y) \quad (5b)$$

Where $\Gamma_+(\omega_m)$ and $\Gamma_-(\omega_m)$ corresponds to a positive and negative first derivative PL signals respectively obtained from phase locked modulation field with σ^- and σ^+.

The $+\hbar$ and $-\hbar$ angular momenta of circularly polarized photons σ^- and σ^+ respectively allow only transitions between states with different quantum numbers. Conservation of angular momentum impose that $\Delta m_s = \pm 1$, thus in NV^- centers with S = 1, this implies that the only allowed transitions are 0 → -1 and 0 → -1.

The quantity $\Gamma_+ - \Gamma_-$ is called dichroic signal and it is related to the magnetic circular dichroic (MCD) technique which describes the differential absorption of circularly polarized radiation due to spin-dependent transitions in spin-split empty states. MCD relies on electric-dipole transitions which interact with the spin part via spin-orbit coupling. In this study the B_1 field is used to drive magnetic-dipole transitions and $\Gamma_+ - \Gamma_-$ is introduced to explain the differential contribution of the 0 → +1 and 0 → -1 transitions induced by the σ^- and σ^+ microwave polarizations in the ODMR-CD spectrum.

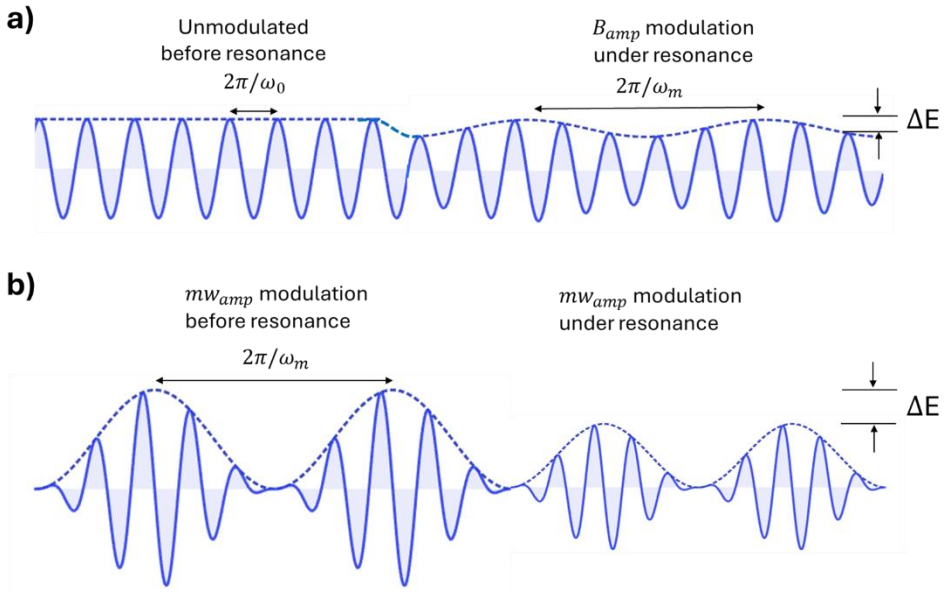

Figure 4 Microwave signal before and during resonance absorption for magnetic field (**a**) and microwave amplitude (**b**) modulation. The absorption energy ΔE is indicated along with the magnetic field and microwave modulation frequencies.

PROOF-OF-CONCEPT

The above observations indicate that the sign of the ODMR-CD spectral lines and hence of the magnetic field modulation phase is locked to a spin transition. Based on this phenomenon the ODMR spectrum emerges as dichroic signal, and it can be used for real time detection of magnetic field directions as explained below.

In the ODMR-CD spectrum the 0 → +1 and 0 → -1 transitions show up opposite signs thus enabling their identification for any arbitrary orientation of the crystal. Upon crystal rotation, each NV^- site experiences a different magnetic field intensity and directions (i.e. $\vec{B}_{NV}$ parallel or antiparallel to the NV^- spin axis). For a fixed orientation, by reversing the magnetic field, the role of the left and right circular polarization is swapped along with the spin transitions of the states involved. Because the modulation phase is locked to the spin transition, the sign of each line will be reversed. From another perspective, each specific spin transition shows always the same ODMR-CD sign regardless the sign of the magnetic field projection $+\vec{B}_{NV}$ or $-\vec{B}_{NV}$. This mechanism allows to detect the polarities of the magnetic field by simply monitoring the sign of a particular ODMR-CD resonance line of one of the four inequivalent NV^- sites. Leveraging on this mechanism a method is provided for reading the polarity an external magnetic field. A proof-of-concept is shown in **Figure 5**. An square like positive and negative voltage is applied to a coil placed in proximity of the diamond microcrystal. A current into the coil generates AC magnetic fields to the sample with 1Hz frequency, while an ODMR-CD signal is monitored as function of time at a fixed resonance frequency υ_r = 2.866 MHz. The resonance frequency it is previously determined by measuring the ODMR-CD spectrum with DC voltage applied to the coil. When recording the ODMR-CD spectrum with B_{mod}, the lock-in signal alternates with the same frequency of the square-wave between positive and negative signals thus enabling real-time detection of magnetic field directions. For comparison, the ODMR spectrum with MW_{mod} remains constant albeit a small

amplitude variation is observed due to the slight asymmetry of the magnetic field between parallel and anti-parallel directions.

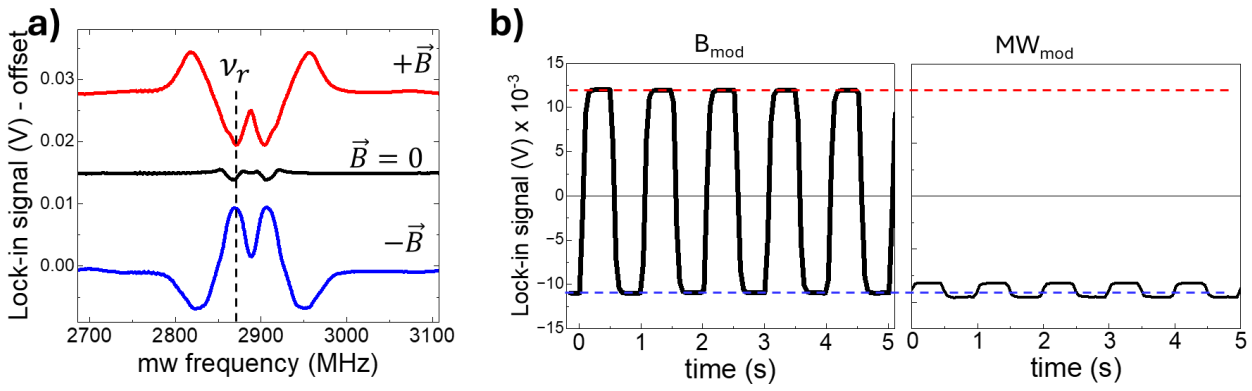

Figure 5. Proof-of-concept for real time detection of switching magnetic fields at 1Hz frequency with B_{mod} and MW_{mod} (**b**) for a fixed resonance frequency ν_r indicated in **(a)**.

CONCLUSIONS

In conclusion, on the one hand a new magnetic resonance phenomenon, here dubbed as Optically Detected Magnetic Resonance – Circular Dichroism (ODMR) is observed for the first time where magnetic resonance spectral signals result from circular dichroism of the exciting microwave radiation. On the other hand, ODMR-CD has been found to deploy NV^- centers in diamond as sensor for direct static and dynamic detection of magnetic field polarities which can be implemented to spatial and temporal mapping of the magnetization spatial distribution and dynamics. Unlike other methods, ODMR-CD does not have constraints for specific crystal orientation, and does not requires an applied external field.[26] Overall, these findings unlock a new degree of freedom in NV^- centers in diamond and extend the range of information that can be extracted from quantum magnetometry and quantum imaging applications. Potentially, ODMC-CD applied to NV^- centers in diamond might unfold new a new range of applications in medical and material science quantum technologies.[27, 28]

MATERIALS AND METHODS

Materials: 150 micron Red Fluorescent Microdiamond with concentration of NV^- ~ 2.5-3 ppm were purchased from Adámas NanoTechnologies Inc. A single crystal was glued on a microstripline.

Optical set-up: A diode pumped solid state (DPSS) laser (Thorlabs DJ532-40) mounted on a current and temperature controller (Thorlabs LDM56F and LDC200C) was used as optical excitation source. The laser beam was directed with a dichroic mirror to a 10x objective with nominal aperture 0.25. The photoluminescence was detected with a silicon photodiode, 350 - 1100 nm, (Thorlabs, SM1PD1B), amplified with a transimpedance photocurrent amplifier (Thorlabs PDA200C) and sent to a MOKU:GO (Liquid Instruments) reconfigurable FPGA oscilloscope/lock in amplifier interfaced with a PC.

Microwave module: a microwave module was assembled with a ADF4351 generator (35 – 4400 MHz) controlled by microprocessor for adjustable frequency sweeps.[29] An SPDT rf switch was used for fast microwave power modulation for MW_{mod} and the microwave signal was 40 dB broadband amplified (max output power 100mW) before feeding a broad band microstripline realized on a single face copper board and FR4 dielectric with thicknesses of 35µm and 1.6mm respectively and terminated with 50 Ω load.

Magnets. NdFeB permanent magnets (Garnet srl) and home-made coils with N=1000 turns and diameter 3cm.

Data acquisition: The photoluminescence was detected on channel 1 of the oscilloscope as function of time while sweeping the microwave frequency whose start and stop frequency sweep logic input is fed into channel 2. The ODMR spectrum is built up by time to frequency conversion. Lock-in

detection was made with time constant 20 ms (12dB/octave) and modulation frequency of 1KHz (see **Figure S2**).

Data were analysed with *Origin professional* and *Matlab*.

Simulations: The spectra were simulated with EasySpin toolbox.[30] The σ^+ and σ^- spectra have been obtained from the diagonalization of the spin-Hamiltonian[24]:

$$\hat{H} = g\mu_B \mathbf{B}\hat{\mathbf{S}} + D(\hat{S}_z^2 + S(S+1)) + E(\hat{S}_x^2 + \hat{S}_y^2) + \sum \hat{\boldsymbol{S}} A \hat{\boldsymbol{I}}, \quad (1)$$

where g is the spectroscopic g-value, μ_B is the Bohr magneton, $\boldsymbol{B}$ is the magnetic field vector, $\hat{\boldsymbol{S}}$ and $\hat{\boldsymbol{I}}$ are the electron and nuclear spin operators, D and E are the zero-field splitting parameters and A_i is the hyperfine splitting between the triplet exciton and the i-th nuclei. The first term is the Zeeman interaction, the second and third terms the zero field splitting and the third term accounts for the hyperfine interactions. Fitting parameters for the spectrum in **Figure 2a** where: $S = 1, g = 2, D = 2887MHz, E = 7MHz, A = 2.5MHz, peak-to-peak\ linewidth = 2.3MHz, B = 3.28mT, crystal\ symmetry = Fd-3m, Euler\ angles: [\alpha,\ \beta, \gamma] = [150°, 110°, 28°]$, $microwave\ propagation\ direction: k \parallel z$. The result of the simulation proofs that the spectrum originates from negatively charged NV^- center in diamond with *Fd-3m* crystal symmetry resulting in four inequivalent sites due to the random substitution of a nitrogen atom next to a vacancy in a tetrahedral symmetry.

The spectra in **Figure 2c** where simulated by using the Euler angles as fitting parameters. The external magnetic field was varied by less than 2.4% around the average value of 2.8 mT to account for small misalignment of the microcrystal from perfect central position of the rotating permanent magnet. The external magnetic field was experimentally measured with an Hall probe and reported to be around 3 .0 ± 0.5 mT and found to be consistent with the values used for the simulations.

DATA AVAILABLITY

Data will be made available on request.

DECLARATION OF COMPETING INTEREST

The authors declare that they have no known competing financial interests or personal relationships that could have appeared to influence the work reported in this paper.

ACKNOWLEDGEMENTS

F.M. gratefully acknowledge financial support by Rete Interdipartimentale di Spettroscopia (project BIR2021) through the “fondi per le grandi attrezzature” University of Milano-Bicocca and PNRR MUR project (PE0000023-NQSTI).

REFERENCES

(1) Doherty, M. W.; Manson, N. B.; Delaney, P.; Jelezko, F.; Wrachtrup, J.; Hollenberg, L. C. L. The nitrogen-vacancy colour centre in diamond. *Physics Reports-Review Section of Physics Letters* **2013**, *528* (1), 1-45.

(2) Kurtsiefer, C.; Mayer, S.; Zarda, P.; Weinfurter, H. Stable Solid-State Source of Single Photons. *Phys. Rev. Lett.* **2000**, *85* (2), 290-293.

(3) Balasubramanian, G.; Neumann, P.; Twitchen, D.; Markham, M.; Kolesov, R.; Mizuochi, N.; Isoya, J.; Achard, J.; Beck, J.; Tissler, J.; et al. Ultralong spin coherence time in isotopically engineered diamond. *Nat. Mater.* **2009**, *8* (5), 383-387.

(4) Zheng, H. J.; Xu, J. Y.; Iwata, G. Z.; Lenz, T.; Michl, J.; Yavkin, B.; Nakamura, K.; Sumiya, H.; Ohshima, T.; Isoya, J.; et al. Zero-Field Magnetometry Based on Nitrogen-Vacancy Ensembles in Diamond. *Physical Review Applied* **2019**, *11* (6).

(5) Michl, J.; Steiner, J.; Denisenko, A.; Bülau, A.; Zimmermann, A.; Nakamura, K.; Sumiya, H.; Onoda, S.; Neumann, P.; Isoya, J.; et al. Robust and Accurate Electric Field Sensing with Solid State Spin Ensembles. *Nano Lett.* **2019**, *19* (8), 4904-4910.

(6) Laraoui, A.; Aycock-Rizzo, H.; Gao, Y.; Lu, X.; Riedo, E.; Meriles, C. A. Imaging thermal conductivity with nanoscale resolution using a scanning spin probe. *Nat. Commun.* **2015**, *6*.

(7) Doherty, M. W.; Struzhkin, V. V.; Simpson, D. A.; McGuinness, L. P.; Meng, Y. F.; Stacey, A.; Karle, T. J.; Hemley, R. J.; Manson, N. B.; Hollenberg, L. C. L.; et al. Electronic properties and metrology applications of the diamond NV^- center under pressure. *Phys. Rev. Lett.* **2014**, *112* (4).

(8) Dutt, M. V. G.; Childress, L.; Jiang, L.; Togan, E.; Maze, J.; Jelezko, F.; Zibrov, A. S.; Hemmer, P. R.; Lukin, M. D. Quantum register based on individual electronic and nuclear spin qubits in diamond. *Science* **2007**, *316* (5829), 1312-1316.

(9) Schirhagl, R.; Chang, K.; Loretz, M.; Degen, C. L. Nitrogen-Vacancy Centers in Diamond: Nanoscale Sensors for Physics and Biology. In *Annual Review of Physical Chemistry, Vol 65*, Johnson, M. A., Martinez, T. J. Eds.; Annual Review of Physical Chemistry, Vol. 65; 2014; pp 83-105.

(10) Boretti, A.; Rosa, L.; Blackledge, J.; Castelletto, S. Nitrogen-vacancy centers in diamond for nanoscale magnetic resonance imaging applications. *Beilstein Journal of Nanotechnology* **2019**, *10*, 2128-2151.

(11) Ajoy, A.; Cappellaro, P. Stable three-axis nuclear-spin gyroscope in diamond. *Phys. Rev. A* **2012**, *86* (6).

(12) Christensen, D. V.; Staub, U.; Devidas, T. R.; Kalisky, B.; Nowack, K. C.; Webb, J. L.; Andersen, U. L.; Huck, A.; Broadway, D. A.; Wagner, K.; et al. 2024 roadmap on magnetic microscopy techniques and their applications in materials science. *Journal of Physics-Materials* **2024**, *7* (3).

(13) Neupane, M.; Belopolski, I.; Hosen, M. M.; Sanchez, D. S.; Sankar, R.; Szlawska, M.; Xu, S. Y.; Dimitri, K.; Dhakal, N.; Maldonado, P.; et al. Observation of topological nodal fermion semimetal phase in ZrSiS. *Phys. Rev. B* **2016**, *93* (20).

(14) Casola, F.; van der Sar, T.; Yacoby, A. Probing condensed matter physics with magnetometry based on nitrogen-vacancy centres in diamond. *Nature Reviews Materials* **2018**, *3* (1).

(15) Balasubramanian, G.; Chan, I. Y.; Kolesov, R.; Al-Hmoud, M.; Tisler, J.; Shin, C.; Kim, C.; Wojcik, A.; Hemmer, P. R.; Krueger, A.; et al. Nanoscale imaging magnetometry with diamond spins under ambient conditions. *Nature* **2008**, *455* (7213), 648-U646.

(16) Rondin, L.; Tetienne, J. P.; Hingant, T.; Roch, J. F.; Maletinsky, P.; Jacques, V. Magnetometry with nitrogen-vacancy defects in diamond. *Rep. Prog. Phys.* **2014**, *77* (5).

(17) Chipaux, M.; Tallaire, A.; Achard, J.; Pezzagna, S.; Meijer, J.; Jacques, V.; Roch, J. F.; Debuisschert, T. Magnetic imaging with an ensemble of nitrogen vacancy-centers in diamond. *European Physical Journal D* **2015**, *69* (7).

(18) Cavenett, B. C. Optically detected magnetic resonance (ODMR) investigation of recombination processes in semiconductors. *Adv. Phys.* **1981**, *30* (4), 475-538.

(19) Luo, J. L.; Geng, Y. F.; Rana, F.; Fuchs, G. D. Room temperature optically detected magnetic resonance of single spins in GaN. *Nat. Mater.* **2024**, *23* (4).

(20) Baranov, P. G.; von Bardeleben, H. J. Semiconductors as Studied by Magnetic Resonance Methods. *Appl. Magn. Reson.* **2010**, *39* (1-2), 1-2.

(21) Stohr, J., Siegmann, H.C. Magnetism. From fundamentals to nanoscale dynamics. Springer-Verlag: Berlin, 2006.

(22) Moro, F.; Moret, M.; Ghirri, A.; del Aguila, A. G.; Kubozono, Y.; Beverina, L.; Cassinese, A. Room-temperature optically detected magnetic resonance of triplet excitons in a pentacene-doped picene single crystal. *J. Mater. Res.* **2022**, *37* (6), 1269-1279.

(23) Babunts, R. A.; Kramushchenko, D. D.; Gurin, A. S.; Bundakova, A. P.; Muzafarova, M. V.; Badalyan, A. G.; Romanov, N. G.; Baranov, P. G. Features of High-Frequency EPR/ESE/ODMR Spectroscopy of NV-Defects in Diamond. *Physics of the Solid State* **2020**, *62* (11), 2024-2032.

(24) Abragam, A.; Bleaney, B. *Electron paramagnetic resonance of transition ions*; Oxford University Press, 1970.

(25) Poole, P. C. *Electron spin resonance: A comprensive treatise on experimental techniques.*; New York J. Wiley, 1996.

(26) Prananto, D.; Kikuchi, D.; Hayashi, K.; Kainuma, Y.; An, T. Imaging of stray magnetic field vectors from a magnetic particle with an ensemble of nitrogen-vacancy centers in diamond. *Jpn. J. Appl. Phys.* **2019**, *58*.

(27) Barry, J. F.; Turner, M. J.; Schloss, J. M.; Glenn, D. R.; Song, Y.; Lukin, M. D.; Park, H.; Walsworth, R. L. Optical magnetic detection of single-neuron action potentials using quantum defects in diamond. *Proc. Natl. Acad. Sci. U.S.A.* **2016**, *113* (49), 14133-14138.

(28) Boto, E.; Holmes, N.; Leggett, J.; Roberts, G.; Shah, V.; Meyer, S. S.; Muñoz, L. D.; Mullinger, K. J.; Tierney, T. M.; Bestmann, S.; et al. Moving magnetoencephalography towards real-world applications with a wearable system. *Nature* **2018**, *555* (7698), 657-+.

(29) Stegemann, J.; Peters, M.; Horsthemke, L.; Langels, N.; Glösekötter, P.; Heusler, S.; Gregor, M. Modular low-cost 3D printed setup for experiments with NV centers in diamond. *European Journal of Physics* **2023**, *44* (3).

(30) Stoll, S.; Schweiger, A. EasySpin, a comprehensive software package for spectral simulation and analysis in EPR. *J. Magn. Reson.* **2006**, *178* (1), 42-55.